J. Fluid Mech. (2005), *vol.* 541, *pp.* 65–90.
doi:10.1017/S002211200500594X Printed in the United Kingdom

Unsteady aerodynamics of fluttering and tumbling plates

By A. ANDERSEN[1], U. PESAVENTO[2] AND Z. JANE WANG[1]

[1]Cornell University, Department of Theoretical and Applied Mechanics, Ithaca, NY 14853, USA

[2]Cornell University, Department of Physics, Ithaca, NY 14853, USA

(Received 13 October 2004 and in revised form 23 May 2005)

We investigate the aerodynamics of freely falling plates in a quasi-two-dimensional flow at Reynolds number of 10^3, which is typical for a leaf or business card falling in air. We quantify the trajectories experimentally using high-speed digital video at sufficient resolution to determine the instantaneous plate accelerations and thus to deduce the instantaneous fluid forces. We compare the measurements with direct numerical solutions of the two-dimensional Navier–Stokes equation. Using inviscid theory as a guide, we decompose the fluid forces into contributions due to acceleration, translation, and rotation of the plate. For both fluttering and tumbling we find that the fluid circulation is dominated by a rotational term proportional to the angular velocity of the plate, as opposed to the translational velocity for a glider with fixed angle of attack. We find that the torque on a freely falling plate is small, i.e. the torque is one to two orders of magnitude smaller than the torque on a glider with fixed angle of attack. Based on these results we revise the existing ODE models of freely falling plates. We get access to different kinds of dynamics by exploring the phase diagram spanned by the Reynolds number, the dimensionless moment of inertia, and the thickness-to-width ratio. In agreement with previous experiments, we find fluttering, tumbling, and apparently chaotic motion. We further investigate the dependence on initial conditions and find brief transients followed by periodic fluttering described by simple harmonics and tumbling with a pronounced period-two structure. Near the cusp-like turning points, the plates elevate, a feature which would be absent if the lift depended on the translational velocity alone.

1. Introduction

Leaves, tree seeds, and paper cards which flutter (oscillate from side to side) or tumble (rotate and drift sideways) are beautiful everyday examples of solid objects moving in a fluid. To predict their complex trajectories requires knowledge of the instantaneous fluid forces. Although determining the forces on a moving geometry in a fluid is a classical problem, only few analytical results exist and they are in special limits such as Stokes flow and inviscid irrotational flow around a steadily translating airfoil. In these steady flows, the fluid forces on a given object depend purely on the kinematic variables, e.g. the translational velocity and the angle of attack in the case of a simple glider. In contrast, most objects moving in a fluid encounter unsteady flows for which it is not clear to what degree quasi-steady models based on inviscid theory apply.

We choose to study freely falling plates for three reasons. First, it is a natural towing tank experiment with gravity being the driving force. Because the plates fall freely, the net force is directly related to the plate acceleration, which can be determined by

tracking the motion with high-speed digital video. This gives us a method for quantifying simultaneously the instantaneous kinematics and the fluid forces, thus providing data to test models of fluid forces. In addition, it is straightforward to generate a wide range of complex motions by changing the properties of the plates such as the thickness-to-width ratio of the plate cross-section. Second, the unconstrained dynamics of freely falling plates driven by gravity is interesting in its own right, and it is analogous to problems such as seed dispersal by wind (McCutchen 1977; Augspurger 1986) and air bubbles rising freely in a liquid (Magnaudet & Eames 2000). Improved force models have important applications for these complex problems, e.g. to elucidate instability mechanisms and transitions related to change in bubble geometry and boundary conditions. Third, our study is in part motivated by our interest in flapping flight. There has been much recent progress in studies of the unsteady forces on flapping wings with wing kinematics similar to those of flying insects in flapping flight (Weis-Fogh & Jensen 1956; Ellington 1984; Dickinson 1996; Sane 2003; Wang 2005). From this perspective, studies of freely falling plates give us access to a different family of periodic solutions, where the external driving force is prescribed instead of the wing kinematics.

Studies of freely falling plates have a long history starting with Maxwell (1854) who described tumbling qualitatively before the development of classical aerodynamics. However, most experiments have focused on qualitative and average properties and not on deducing the instantaneous fluid forces (Dupleich 1941; Willmarth, Hawk & Harvey 1964; Smith 1971; Field *et al.* 1997; Belmonte, Eisenberg & Moses 1998; Mahadevan, Ryu & Samuel 1999). Dupleich (1941) measured the angle of descent and the average tumbling frequency as functions of wing loading and ratio between plate length and width. Willmarth *et al.* (1964) measured a phase diagram for falling disks with steady descent, fluttering, and tumbling, and in the limit of small thickness-to-width ratio they found that the final state depends only on the Reynolds number and the dimensionless moment of inertia. Smith (1971) measured a phase diagram for falling plates qualitatively similar to the one for falling disks, Field *et al.* (1997) made further experiments on freely falling disks with apparently chaotic motion, Belmonte *et al.* (1998) quantified the transition from fluttering to tumbling in a quasi two-dimensional experiment, and Mahadevan *et al.* (1999) observed a scaling law for the dependence of the rotational speed on the width of a tumbling card. Jones & Shelley (2005) proposed a falling card model based on inviscid theory and the unsteady Kutta condition, but the method has so far not been implemented numerically to model periodic fluttering and tumbling.

Tumbling has also been studied in the context of free and fixed-axis auto-rotation as reviewed by Lugt (1983). Wind-tunnel experiments on fixed-axis auto-rotation of plates (Smith 1971; Skews 1990) and polygonal objects (Skews 1991) were carried out at Reynolds numbers in the range 10^4–10^5. Fixed-axis auto-rotation and tumbling of a freely falling plate have some similarities, but there are significant differences between the two phenomena. The most important difference is that fixed-axis auto-rotation involves only the rotational degree of freedom of the plate, and thus the coupling between translation and rotation is absent. Therefore it is not clear *a priori* how results on the two different types of auto-rotation are related.

Our main goal in this paper is to describe the motion of freely falling rigid plates based on detailed measurement of the plate trajectories and from this to learn about the instantaneous fluid forces. We record the trajectories using high-speed digital video, which gives us sufficient temporal and spatial resolution to obtain instantaneous translational and rotational velocities and to extract the instantaneous fluid forces and

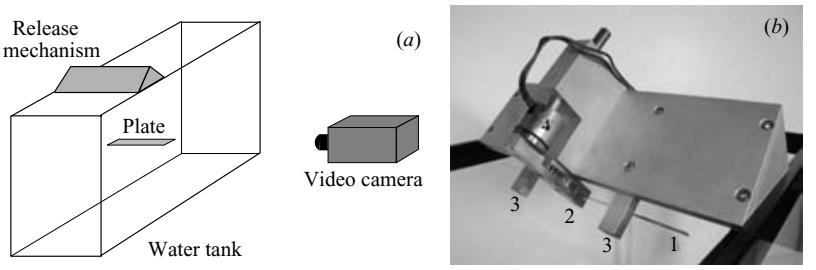

FIGURE 1. The experimental apparatus; (*a*) the transparent glass container, the release mechanism, the falling plate, and the high-speed digital video camera shown schematically; (*b*) the release mechanism mounted on top of the container. The aluminum plate (1) is held at its midpoint by the clamp (2) below the water surface and it is aligned horizontally using the two bars (3). The plate is released when the clamp is opened using the small electromagnet (4).

torques on the plates. The experiment is essentially two-dimensional, and it allows us to compare the measurements with direct numerical simulations of the Navier–Stokes equation for a rigid body falling in a two-dimensional flow. In this way we supplement the experiment with numerical flow visualizations. We describe the computed wake structure and compare the measured and the computed fluid forces.

The measured and the computed forces allow a direct test of the force models proposed in the literature (Tanabe & Kaneko 1994; Mahadevan 1996; Belmonte *et al.* 1998; Pesavento & Wang 2004). Our force model is based on Kirchhoff's equations governing the motion of a solid in an inviscid fluid (Lamb 1945). A missing quantity in inviscid theory is the instantaneous circulation. We test the recent model of the circulation by Pesavento & Wang (2004), which contains both translational and rotational contributions. We compare the model predictions with the measured forces, and discuss the force contributions due to acceleration, translation, and rotation.

2. Experimental and numerical methods

2.1. *Experimental setup and image analysis*

We measure the trajectories of small aluminium plates which fall in a water tank in an essentially two-dimensional experiment. The experiment is conducted using a rectangular glass container which is 30 cm wide, 45 cm high, and 75 cm long, see figure 1(*a*). The container is filled with water, and a release mechanism on top of the container allows us to drop the plates below the water surface with well-controlled initial conditions. The release mechanism consists of a metal clamp which holds the plates at their midpoint and opens using a small electromagnet as shown in figure 1(*b*).

The plates are 19 cm long and between 0.6 cm and 1.1 cm wide. The large length-to-width ratios of between 15 and 30 make the influence of three-dimensional effects at the ends negligible. In this way the setup is different from the one used by Smith (1971) in which the length to width ratio was between 3 and 4, and tip plates were used to reduce three-dimensional effects. In our experiment the plates are released so that they rotate about their axis of symmetry in the length direction and fall with two-dimensional trajectories in the plane normal to the length direction. The plates thus fall through the water without any constraints on their motion and without touching the walls of the container. This feature makes the setup different from the one used by Belmonte *et al.* (1998) in which the container is narrow and the plates touch the sides of the container to constrain their motion to be two-dimensional. The plate

motion depends sensitively on the drag and the dissipative fluid torque, and any additional damping from friction between the plate and the container walls could affect the behaviour at the turning points in particular. In the present experiment such additional damping is absent since there are 5 cm wide spacings between the plate tips and the container walls.

We record the trajectories using high-speed digital video at 400 to 500 frames per second. The framerate is sufficient to resolve both the translational and the rotational motion during all parts of the descent, including the turning points which are dominated by fast rotational motion. We position the camera on one side of the transparent glass container, see figure 1(*a*), and illuminate a white background homogeneously on the opposite side of the container. In each frame we observe the dark plate cross-section on the white background and identify the centre and the orientation of the plate cross-section. The measured trajectories are smooth, and we are able to obtain instantaneous velocities using a finite difference scheme. However, we have to filter out high-frequency noise using the Fourier transform to obtain instantaneous accelerations. In the following we present velocities and forces where high-frequency noise is filtered out.

2.2. *Direct numerical solutions of the Navier–Stokes equation*

We solve the two-dimensional Navier–Stokes equation for the flow around the plate in the vorticity–stream function formulation. In the case of a symmetric and freely falling plate the fluid force acts near the centre of mass, and the resulting torque relative to the centre of mass is small. The accuracy of the solution of the coupled system is therefore determined by the error in the pressure torque. To obtain sufficient accuracy we use a fourth-order finite difference scheme introduced by E & Liu (1996) and a body-fitted computational grid generated by a conformal mapping. To avoid singularities at the corners of the two-dimensional plates we use an elliptical cross-section and the method applied by Wang (2000) for the two-dimensional flow around a flapping wing with prescribed kinematics. In body-fixed elliptical coordinates (μ, ϕ) we have

$$\frac{\partial(S\omega)}{\partial t} + (\sqrt{S}\boldsymbol{u}\cdot\nabla)\omega = \nu\nabla^2\omega, \tag{2.1}$$

$$\nabla\cdot(\sqrt{S}\boldsymbol{u}) = 0, \tag{2.2}$$

where $\boldsymbol{u}$ is the velocity field, ω the vorticity field, and ν the kinematic viscosity of the fluid. The scaling factor

$$S(\mu, \phi) = c^2(\cosh^2\mu - \cos^2\phi), \tag{2.3}$$

is associated with the conformal mapping from the exterior of the ellipse with major axis $l = 2c\cosh\mu_0$ to a semi-infinite strip, where $\mu = \mu_0$ at the boundary of the ellipse

$$x + \mathrm{i}y = c\cosh(\mu + \mathrm{i}\phi). \tag{2.4}$$

The mapping concentrates grid points at the edges of the plate and casts the Navier–Stokes equation onto a Cartesian grid, allowing an efficient solver. We use body-fixed coordinates to eliminate spatial interpolation as the plate moves with respect to the fluid. This turns out to be crucial for obtaining long trajectories with freely falling plates.

The pressure and viscous force and torque on a stationary plate can be calculated by integrating the stress tensor along the surface as described by Lugt & Haussling (1974). The contributions from the plate acceleration to the pressure force, $\boldsymbol{F}_p$, and the

pressure torque, τ_p, are given by the $\boldsymbol{a}$ and $\dot{\Omega}$ terms in equations (2.5) and (2.6), and the viscous force, $\boldsymbol{F}_v$, and torque, τ_v, have the same form as for a stationary ellipse:

$$\boldsymbol{F}_p = \nu\rho_f c \int (\sinh\mu_0 \sin\phi, -\cosh\mu_0 \cos\phi)\frac{\partial\omega}{\partial\mu}\,\mathrm{d}\phi + \frac{1}{4}\pi\rho_f lh\boldsymbol{a}, \tag{2.5}$$

$$\tau_p = \frac{1}{2}\nu\rho_f c^2 \int \frac{\partial\omega}{\partial\mu}\sin^2\phi\,\mathrm{d}\phi + \frac{1}{32}\pi\rho_f lh(l^2+h^2)\dot{\Omega}, \tag{2.6}$$

$$\boldsymbol{F}_v = \nu\rho_f c \int \omega(-\cosh\mu_0 \sin\phi, \sinh\mu_0 \cos\phi)\,\mathrm{d}\phi, \tag{2.7}$$

$$\tau_v = \nu\rho_f c^2 \cosh\mu_0 \sinh\mu_0 \int \omega\,\mathrm{d}\phi, \tag{2.8}$$

where ρ_f is the density of the fluid, h is the minor axis of the ellipse, and $\boldsymbol{a}$ and $\dot{\Omega}$ are the translational and the angular acceleration of the plate, respectively. The plate dynamics follows Newton's 2nd law, and the updated plate velocity is fedback to the Navier–Stokes solver through the boundary conditions. With this computational method it typically takes 10 to 20 times longer to resolve the free fall of a plate than to compute the flow past the same plate undergoing a similar but prescribed motion in which the feedback step is not needed. The simulations of freely falling plates discussed in the following are obtained using a 512×1024 grid and were repeated using a 256×512 grid to check the computational accuracy. The results presented hold for both resolutions.

3. Non-dimensional parameters and phase diagram

A freely falling plate is characterized by six dimensional parameters, i.e. the width of the plate, l, the thickness of the plate, h, the density of the plate, ρ_s, the density of the fluid, ρ_f, the kinematic viscosity of the fluid, ν, and the acceleration due to gravity, g. From the six dimensional numbers we form three non-dimensional parameters, i.e. the thickness-to-width ratio, β, the dimensionless moment of inertia, I^*, and the Reynolds number, Re. Specifically we define the thickness-to-width ratio of the plate cross-section

$$\beta = \frac{h}{l}, \tag{3.1}$$

and the dimensionless moment of inertia (Smith 1971)

$$I^* = \frac{32I}{\pi\rho_f l^4}, \tag{3.2}$$

where $\pi\rho_f l^4/32$ is the moment of inertia per length about the axis of symmetry of a cylinder of density ρ_f and diameter l. With rectangular cross-section we have $I^* = 8\rho_s h(l^2+h^2)/(3\pi\rho_f l^3)$ and with elliptical cross-section $I^* = \rho_s h(l^2+h^2)/(2\rho_f l^3)$. We define the Reynolds number using the width of the plate and the descent speed

$$Re = \frac{lV}{\nu}. \tag{3.3}$$

A simple estimate of the average descent speed, V, at intermediate Re gives

$$V \approx \sqrt{2(\rho_s/\rho_f - 1)hg}. \tag{3.4}$$

The estimate is obtained by balancing the buoyancy-corrected gravity, $(\rho_s - \rho_f)hlg$, with the quadratic drag, $\rho_f lV^2/2$. However, Willmarth *et al.* (1964) and Smith (1971)

h (cm)	β	I^*	Re	$\langle v_x \rangle$ (cm s^{-1})	$\langle v_y \rangle$ (cm s^{-1})	$\langle \omega \rangle$ (rad s^{-1})
0.162	1/5	0.48	737	14.2 ± 0.1	-8.1 ± 0.3	25.5 ± 0.3
0.162	1/6	0.39	1770	15.2 ± 0.7	-16.2 ± 2.9	16.1 ± 1.1
0.081	1/8	0.29	837	15.9 ± 0.3	-11.5 ± 0.5	14.5 ± 0.3
0.081	1/14	0.16	1147	19.8 ± 0.3	-9.0 ± 0.2	6.8 ± 0.1

TABLE 1. The thickness h, the non-dimensional parameters β, I^*, and Re, and the measured average horizontal velocity $\langle v_x \rangle$, vertical velocity $\langle v_y \rangle$, and angular velocity $\langle \omega \rangle$. The Reynolds number defined in equation (3.3) is obtained using $\langle v_y \rangle$ and the kinematic viscosity of water at 25° C, i.e. $\nu = 0.0089\,\mathrm{cm^2\,s^{-1}}$. The averages for $\beta = 1/5$ are based on 10 trajectories with 8 periods each, the averages for $\beta = 1/8$ are based on 20 trajectories with 3 periods each, and the averages for $\beta = 1/14$ are based on 10 trajectories with 5 periods each. For the plates with $\beta = 1/6$ and $\beta = 1/14$ we report the averages of the absolute values of v_x and ω.

used the measured value of the average descent speed in the definition of the Reynolds number and we shall follow their convention.

Smith (1971) found a phase diagram for rectangular plates that was qualitatively similar to the phase diagram for circular disks measured by Willmarth *et al.* (1964). The plates descend steadily when Re is below 100, and a transition from fluttering to tumbling takes place with increasing I^* at larger values of Re. Smith (1971) measured the transition value of I^* to be 0.2–0.3, whereas Belmonte *et al.* (1998) found a transition value of 0.4 in their quasi-two-dimensional experiment.

4. Trajectories

The measured trajectories of aluminium plates with different thickness-to-width ratio show a number of interesting characteristics. We use plates with rectangular cross-section and thickness-to-width ratio between $\beta = 1/14$ and $\beta = 1/5$. Both the thickness and the width are therefore potentially important length scales, and we are not in the range of small β studied by Willmarth *et al.* (1964) and Smith (1971). Figure 2 shows the trajectories of three of the four experimental plates, and table 1 summarizes the experiment: a fluttering plate with $\beta = 1/14$, two tumbling plates with $\beta = 1/5$ and $\beta = 1/8$, respectively, and a plate with $\beta = 1/6$ showing apparently chaotic motion.

4.1. *Fluttering*

Figure 2(*a*) shows the trajectory and the solid lines in figure 3 show the velocity components for the fluttering plate with $h = 0.081$ cm and $\beta = 1/14$. The plate oscillates from side to side as it descends with alternating gliding at low angle of attack and fast rotational motion at the turning points. The centre of mass elevates at the turning points, and the turning points are cusp-like since the translational motion almost ceases.

The periodic motion of a fluttering plate is in general complex and not easy to describe by simple functions. However, it is evident from the measured translational velocity components shown in figure 3 that the fluttering of the plate with $\beta = 1/14$ is dominated by the lowest harmonics. The trajectory is well-described by the simple curve

$$x(t) = \frac{V_1}{\Omega} \sin(\Omega t), \tag{4.1}$$

$$y(t) = -V_2 t - \frac{V_3}{2\Omega} \cos(2\Omega t), \tag{4.2}$$

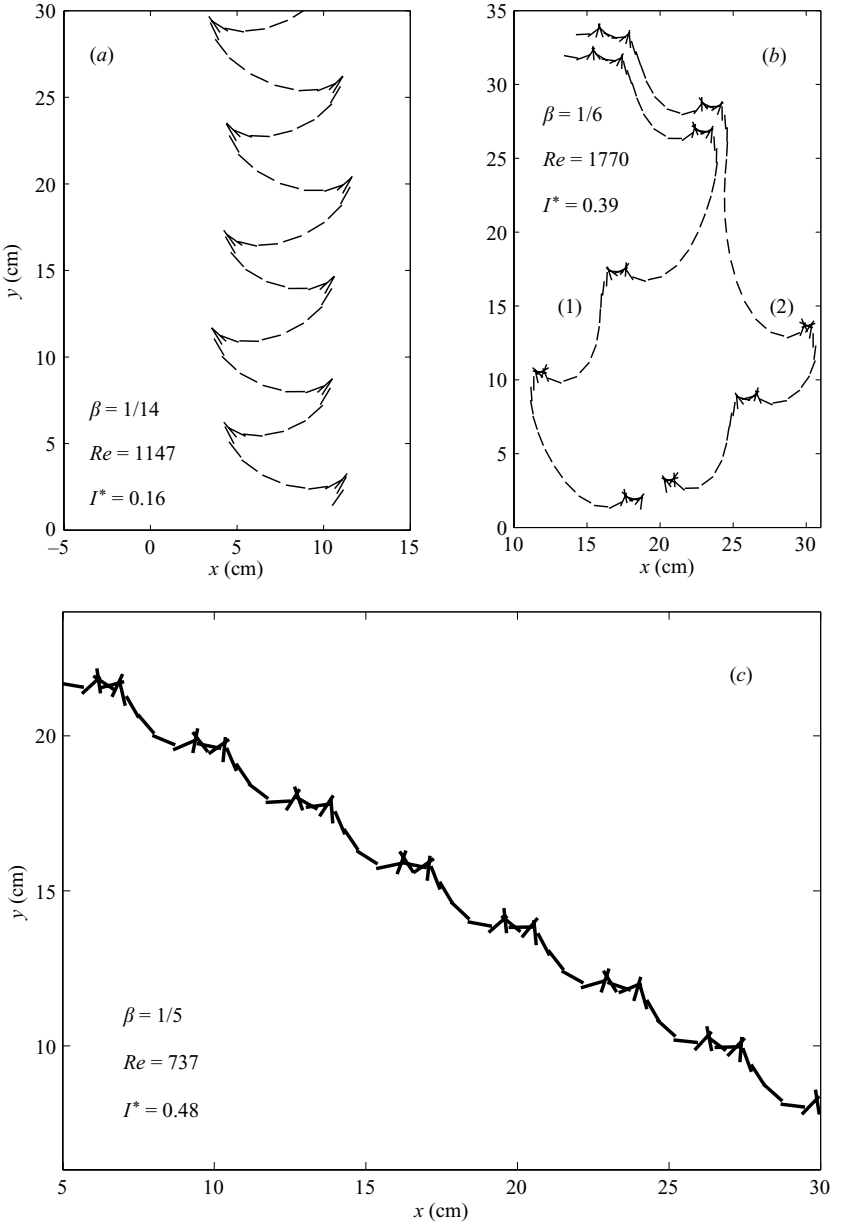

FIGURE 2. Measured plate trajectories: (*a*) the fluttering plate with $h = 0.081$ cm and $\beta = 1/14$, (*b*) two apparently chaotic trajectories for the $h = 0.162$ cm and $\beta = 1/6$ plate, and (*c*) the tumbling plate with $h = 0.162$ cm and $\beta = 1/5$. For clarity the two trajectories in (*b*) are displaced from each other 0.5 cm horizontally and 1.5 cm vertically. The thick line segments show the plate cross-sections with time intervals of 0.04 s in (*a*) and 0.025 s in (*b*) and (*c*).

where Ω, V_1, V_2, and V_3 are constants. The constant Ω is the angular frequency of the periodic motion, V_2 is the average descent speed, and V_1 and V_3 describe the amplitudes of the oscillations in v_x and v_y, respectively. Figure 4 shows the curve (4.1) and (4.2) with the parameters $\Omega = 9.8\,\mathrm{rad\,s^{-1}}$, $V_1 = 32.6\,\mathrm{cm\,s^{-1}}$, $V_2 = 9.1\,\mathrm{cm\,s^{-1}}$, and $V_3 = 14.5\,\mathrm{cm\,s^{-1}}$ obtained from the fits shown by the two dotted lines in figure 3.

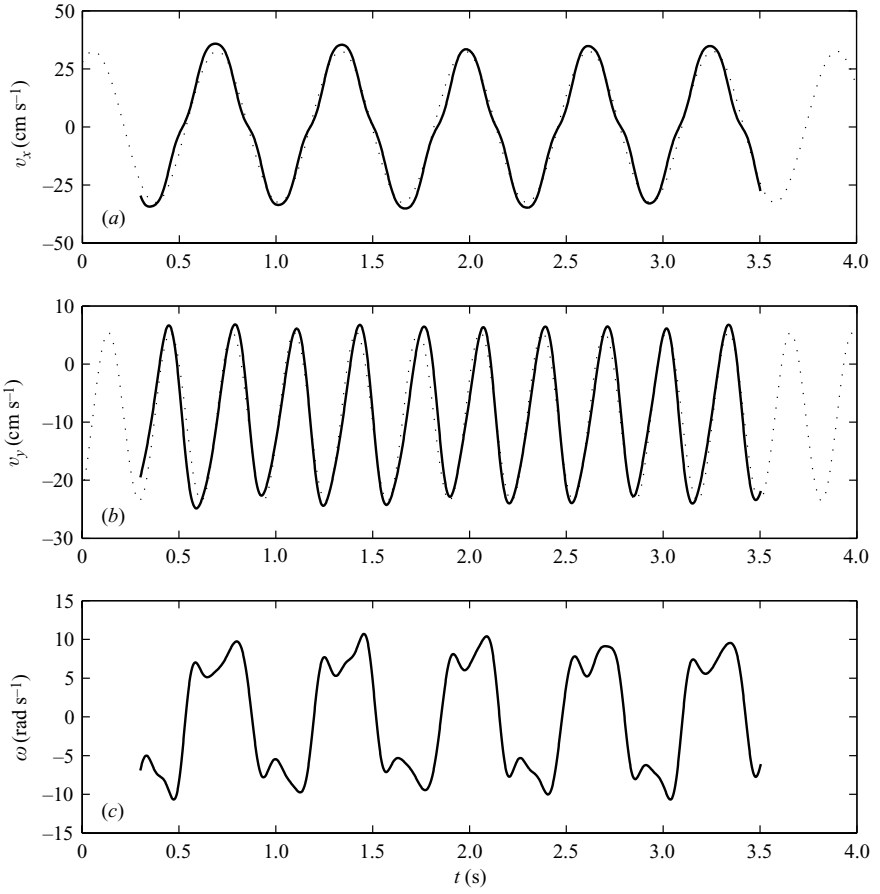

FIGURE 3. The measured velocities (solid lines) for fluttering with $h = 0.081$ cm and $\beta = 1/14$, and the best fits (dotted lines) of the velocity expressions derived from equations (4.1) and (4.2). (*a*) The horizontal velocity component v_x, (*b*) the vertical velocity component v_y, and (*c*) the angular velocity ω. Both v_x and v_y are well-described by a single harmonics, whereas three harmonics are needed to capture the main features of ω with three local extrema for each half-period.

The frequency of the oscillatory component of the vertical velocity is twice the frequency of the oscillatory horizontal velocity component because of the symmetry of the fluttering motion. Any solution with periodic and symmetric side-to-side oscillations and constant average descent speed will therefore in general contain terms like (4.1) and (4.2). A special example of such motion is that of a rigid object with elliptical cross-section in a two-dimensional inviscid flow without gravity and circulation (Lamb 1945). The problem is described by Kirchhoff's equations, and the small-amplitude analytical solution consists of symmetric side-to-side oscillations. However, the phase difference between the two oscillatory components and the rotational motion in the ideal fluid problem are different from the fluttering trajectory of a thin plate falling in a viscous fluid.

4.2. *Tumbling*

Figure 2(*c*) shows the trajectory and figure 5 the velocity components as functions of time for the tumbling plate with $h = 0.162$ cm and $\beta = 1/5$. The plate is released at

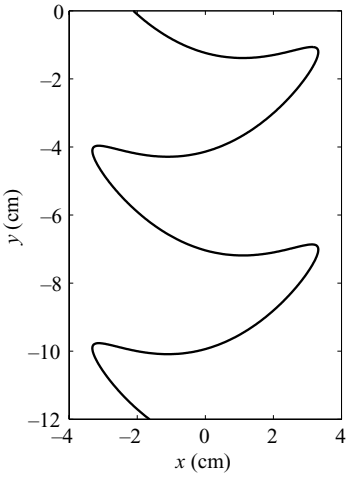

FIGURE 4. The simple analytical curve (4.1) and (4.2) describes the fluttering trajectory for the plate with $\beta = 1/14$ shown in figure 2(*a*). The curve parameters are obtained by fitting the translational velocity components as shown by the two dotted lines in figure 3.

an angle of 60° with the horizontal, and it settles into periodic motion after one to two complete rotations. The periodic motion alternates between short and long gliding segments, and the typical tumbling motion has a pronounced period-two structure. The plate rotates fast at the turning points with angular velocities up to $\omega = 40\,\mathrm{rad\,s^{-1}}$ as shown in figure 5(*c*). The centre of mass elevates following the long gliding segments whereas it does not elevate following the short gliding segments as shown in figure 5(*b*).

4.3. *Apparently chaotic motion*

Figure 2(*b*) shows two typical trajectories for the $h = 0.162\,\mathrm{cm}$ and $\beta = 1/6$ plate with apparently chaotic motion, and figure 6 shows the velocity components as functions of time for plate (1) in figure 2(*b*). The motion in the transition region between fluttering and tumbling alternates between fast complete rotations and segments where the plate glides at low angle of attack for distances up to 15 times the plate width. The two trajectories start with similar initial conditions, but the dynamics is very sensitive to the initial conditions of the plate and the water. Both plates end up almost at rest and oriented vertically after a few complete rotations, and in this state it is undetermined whether the plates will flutter or tumble. Plate (1) therefore glides to the left whereas plate (2) glides to the right. The apparently chaotic motion is radically different from the periodic fluttering and tumbling with short transients, and when the plates are almost at rest and oriented vertically the dynamics is much more sensitive to experimental noise than in the periodic regions. We note that Field *et al.* (1997) observed similar apparently chaotic motion for freely falling disks, whereas apparently chaotic motion was not found in the experiment by Belmonte *et al.* (1998).

In a separate paper we have presented direct numerical simulations at somewhat lower Reynolds number showing a wide transition region between fluttering and tumbling in which the plates flutter periodically but tumble once between consecutive turning points (Andersen, Pesavento & Wang 2005). Within the framework of the quasi-steady model we also analysed the transition between fluttering and tumbling

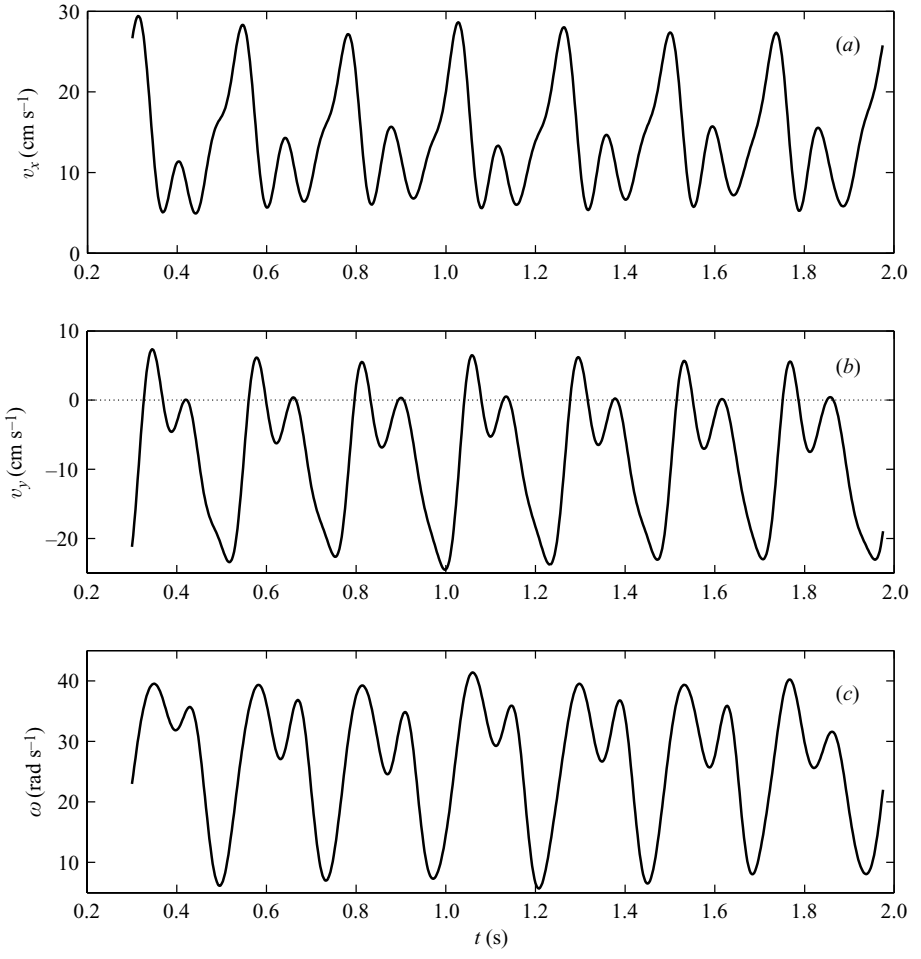

FIGURE 5. Measured velocities as functions of time for the tumbling plate with $h = 0.162$ cm and $\beta = 1/5$. (*a*) The horizontal velocity component, (*b*) the vertical velocity component, and (*c*) the angular velocity. The plate elevates (v_y is positive) after the long gliding segments whereas it does not elevate after the short gliding segments. The local maxima for v_y and ω almost coincide, and we note that v_x is large and ω is small during the long gliding segments.

for plates with small thickness-to-width ratio for which the dimensionless moment of inertia is the relevant control parameter. We identified the transition in the quasi-steady model as a heteroclinic bifurcation, and using the direct numerical simulations we found that the transition between fluttering and tumbling does not always take place via a sequence of chaotic solutions. These results could suggest that the apparently chaotic trajectories are observed in the present experiment because the system is very sensitive to noise in the transition region and that the trajectories only appear to be chaotic due to experimental noise.

4.4. *Comparison between experiment and direct numerical simulations*

To validate and check the measurements and the direct numerical simulations we compare measured and computed trajectories for the tumbling plate with $\beta = 1/8$. We keep the width and the thickness the same in the experiment and the simulations, but the plate in the experiment has rectangular cross-section whereas the plate in the

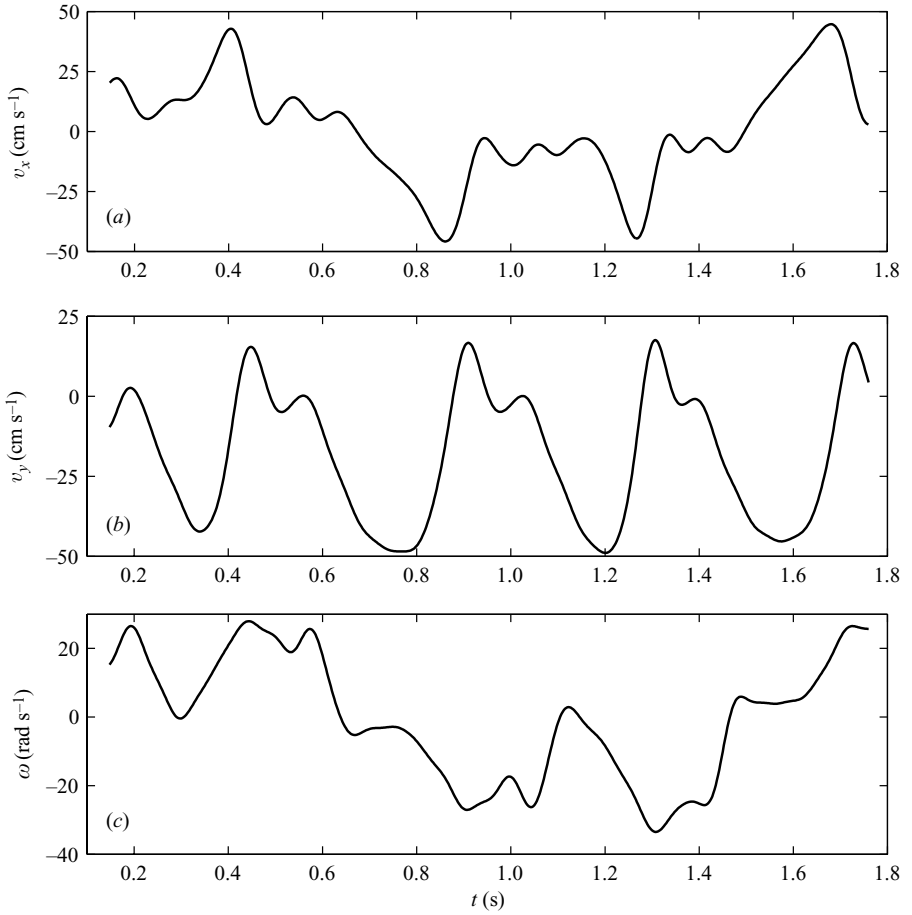

FIGURE 6. Measured velocities as functions of time for the plate with $h = 0.162$ cm and $\beta = 1/6$ displaying irregular motion, see trajectory (1) in figure 2(*b*). (*a*) The horizontal velocity component, (*b*) the vertical velocity component, and (*c*) the angular velocity. The irregular motion involves long gliding segments at low angle of attack with descent velocities up to $v_y = -50\,\mathrm{cm\,s^{-1}}$ followed by centre-of-mass elevation with upward velocities up to $v_y = 20\,\mathrm{cm\,s^{-1}}$.

simulations has elliptical cross-section to take advantage of the conformal mapping (2.4) with no singular corners. Both the mass and the moment of inertia are therefore smaller in the simulations in comparison with the experiment. With the rectangular cross-section we have $I^* = 0.29$ and $Re = 837$ and with the elliptical cross-section $I^* = 0.17$ and $Re = 1025$. The measurements were repeated 20 times with initial conditions set by releasing the plate at an angle of 45° with the horizontal, and the simulations were carried out with the five different sets of initial conditions (I–V) specified in table 2.

Figure 7(*a*) shows the plate trajectories and figure 7(*b*) shows v_x versus v_y for two representative trajectories, one measured and one computed. The trajectories are qualitatively similar, but the period-two structure is more pronounced in the simulations as shown in figure 7(*b*). We ascribe the differences between the trajectories to the differences between the rectangular and the elliptical cross-section. The average velocity components, angular velocity, and angle of descent are reported in table 3.

β	Run	v_x (cm s^{-1})	v_y (cm s^{-1})	ω (rad s^{-1})	θ (deg.)
1/8	I	0.00	0.00	0.00	11.5
–	II	0.00	0.00	−16.50	−11.5
–	III	−8.92	−8.92	0.00	45.3
–	IV	−17.90	−17.90	0.00	45.3
–	V	−35.70	53.40	0.00	45.3
1/4	VI	0.00	0.00	0.00	11.5
–	VII	0.00	0.00	−2.90	−11.5

TABLE 2. Initial conditions for the plates in the direct numerical simulations. I–V: $\beta = 1/8$, $h = 0.081$ cm, $\rho_f = 1.0$ g cm^{-3}, $\rho_s = 2.7$ g cm^{-3}, and $\nu = 0.0089$ cm^2 s^{-1}; VI–VII: $\beta = 1/4$, $h = 0.05$ cm, $\rho_f = 1.0$ g cm^{-3}, $\rho_s = 2.0$ g cm^{-3}, and $\nu = 0.0089$ cm^2 s^{-1}.

	$\langle v_x \rangle$ (cm s^{-1})	$\langle v_y \rangle$ (cm s^{-1})	$\langle \omega \rangle$ (rad s^{-1})	Descent angle (deg.)
Experiment:	15.9 ± 0.3	-11.5 ± 0.5	14.5 ± 0.3	35.8 ± 1.3
Simulation:	15.6 ± 0.2	-7.4 ± 0.3	18.0 ± 0.3	25.3 ± 0.9

TABLE 3. Average velocities $\langle v_x \rangle$ and $\langle v_y \rangle$, angular velocity $\langle \omega \rangle$, and angle of descent for the tumbling plate with $\beta = 1/8$ in the experiment (rectangular cross-section) and in the direct numerical simulations (elliptical cross-section) with initial conditions (I–V) in table 2.

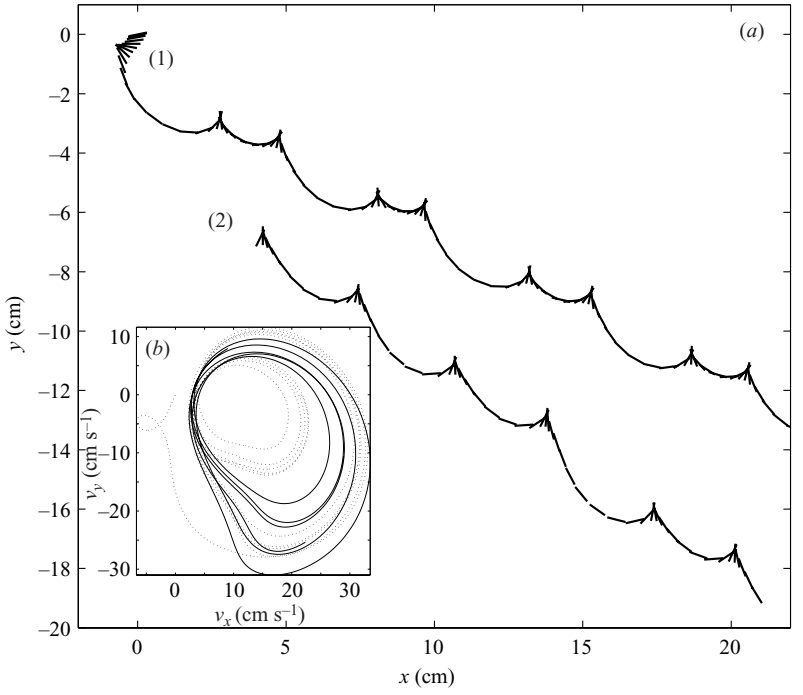

FIGURE 7. Tumbling dynamics with $\beta = 1/8$ from the experiment and the direct numerical simulation with initial condition I in table 2. (*a*) Computed and measured trajectories labelled (1) and (2), respectively, and (*b*) v_x versus v_y: simulation (dotted line) and experiment (solid line). The trajectories are qualitatively similar, and we ascribe the quantitative differences to the difference in geometry between the rectangular and the elliptical cross-section.

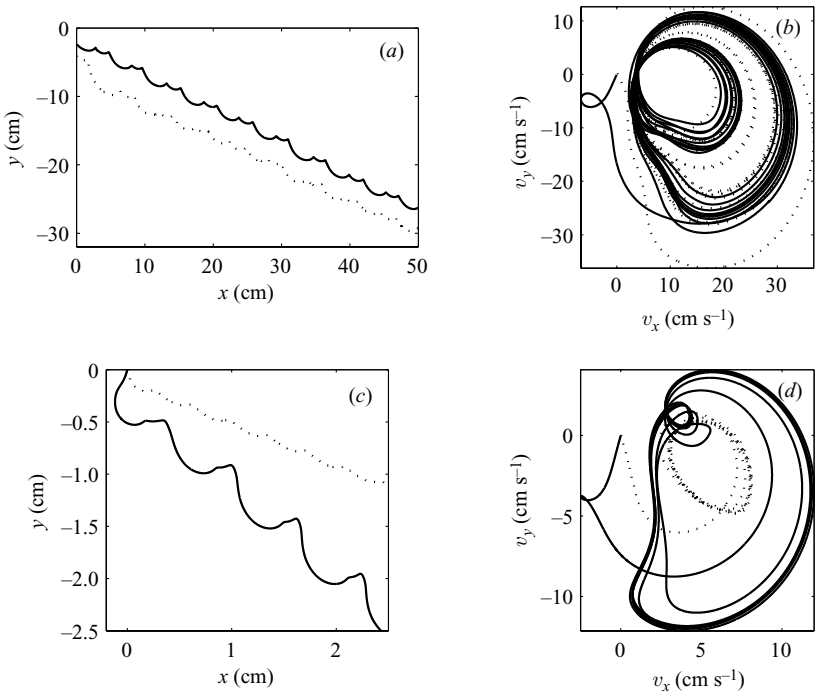

FIGURE 8. Periodic solutions and dependence on initial conditions investigated using direct numerical simulations: (*a*) trajectory and (*b*) v_x versus v_y for a tumbling plate with $\beta = 1/8$, $Re = 1025$, and $I^* = 0.17$ with initial condition I (solid line) and II (dotted line) from table 2; (*c*) trajectory and (*d*) v_x versus v_y for a tumbling plate with $\beta = 1/4$, $Re = 10^2$, and $I^* = 0.36$ with initial condition VI (solid line) and VII (dotted line) from table 2.

The average tumbling frequency in the simulations is 25% higher than the average tumbling frequency in the experiment. The average angle of descent relative to the horizontal is 25.3° in the simulations and 35.8° in the experiments, and the average descent velocity is about 50% larger in the experiments than in the simulations. The standard deviations are comparable in the experiments and in the simulations as reported in table 3.

4.5. *Sensitivity to initial conditions*

Numerically we investigate the dependence on initial conditions by specifying different initial conditions of the plate as summarized in table 2. Figure 8(*a*) shows the trajectories of the plate with $\beta = 1/8$ in two simulations with 10 complete periods and initial conditions I and II from table 2. The initial transients of the two runs are very different, as expected, but after two complete rotations the two trajectories span the same region in the v_x versus v_y plot and exhibit similar period-two dynamics as shown in figure 8(*b*). However, the initial conditions have significant importance in some cases. The apparently chaotic trajectories shown in figure 2(*b*) depend sensitively on the initial conditions, and periodic solutions can also depend sensitively on the initial conditions as shown in figures 8(*c*) and 8(*d*). One trajectory (solid line) displays a pronounced period-two structure whereas the other trajectory (dotted line) displays a period-one structure.

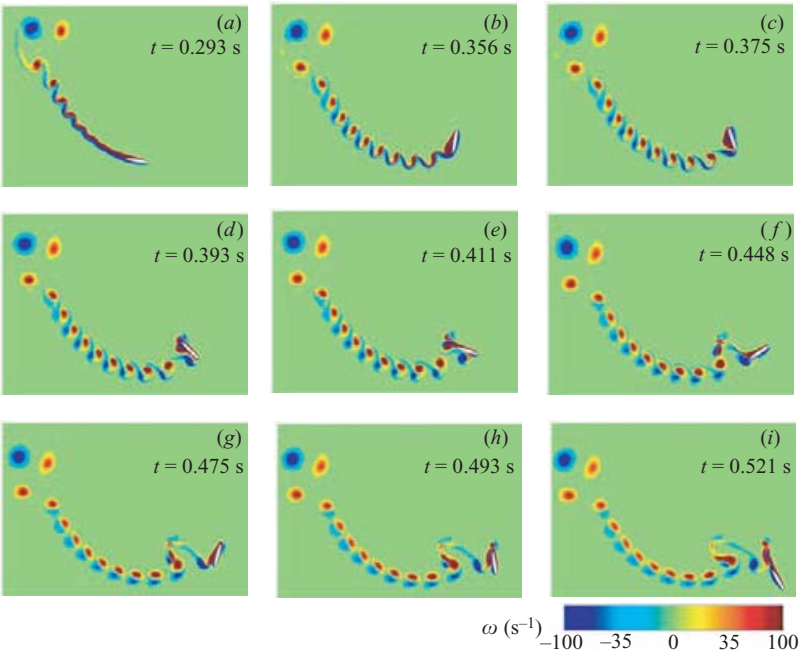

FIGURE 9. The vorticity around the tumbling plate with $\beta = 1/8$, $I^* = 0.17$, and $Re = 1025$. The grid resolution was 512×1024. Positive vorticity in red and negative vorticity in blue: (*a*) onset of the wake instability; (*b*) the instability is fully developed, and the plate has initiated its first turn; (*c*, *d*) a vortex pair is formed as the plate completes its turn; (*e*) the plate glides for a short distance; (*f*–*h*) the plate makes a second 180° turn; and (*i*) the plate resumes gliding.

5. Vortex shedding and wake structure

5.1. *Tumbling*

The wake of the tumbling plate with $\beta = 1/8$ consists of vortices shed at the turning points plus vortex pairs formed by the breakup of the extended wake formed during gliding. Figure 9 shows snapshots of the vorticity field around the plate. The vortex pair in the top left corner of each frame was shed after the initial fluttering transient. The plate starts gliding after the transient, and the trajectory alternates between short and long gliding segments separated by 180° rotations. As the plate initiates a turn, the wake developed during the previous gliding segment becomes unstable and breaks up into vortices with a characteristic size of half the plate width. In addition, two vortices are shed when the plate undergoes a 180° rotation and resumes gliding. The short gliding segments are similar to the long gliding segments except that the wake of the plate has less time to develop and generates fewer vortices as it breaks up.

5.2. *Fluttering*

Figure 10 shows the vorticity field around a fluttering plate with elliptical cross-section, $\beta = 1/18$, $I^* = 0.057$, and $Re = 412$. Numerically we have not resolved the $\beta = 1/14$ fluttering, and to illustrate the wake structure in fluttering we consider an example at somewhat lower Reynolds number. The vortex dipole shed during the initial transient is visible at the top left corner in figure 10(*a*). A similar dipole is shed during the transient of the tumbling plate shown in figure 9. In both cases the plate glides at small angle of attack after the transient until it starts to pitch up and approach the turning point. As the plate pitches up it decelerates, its wake becomes

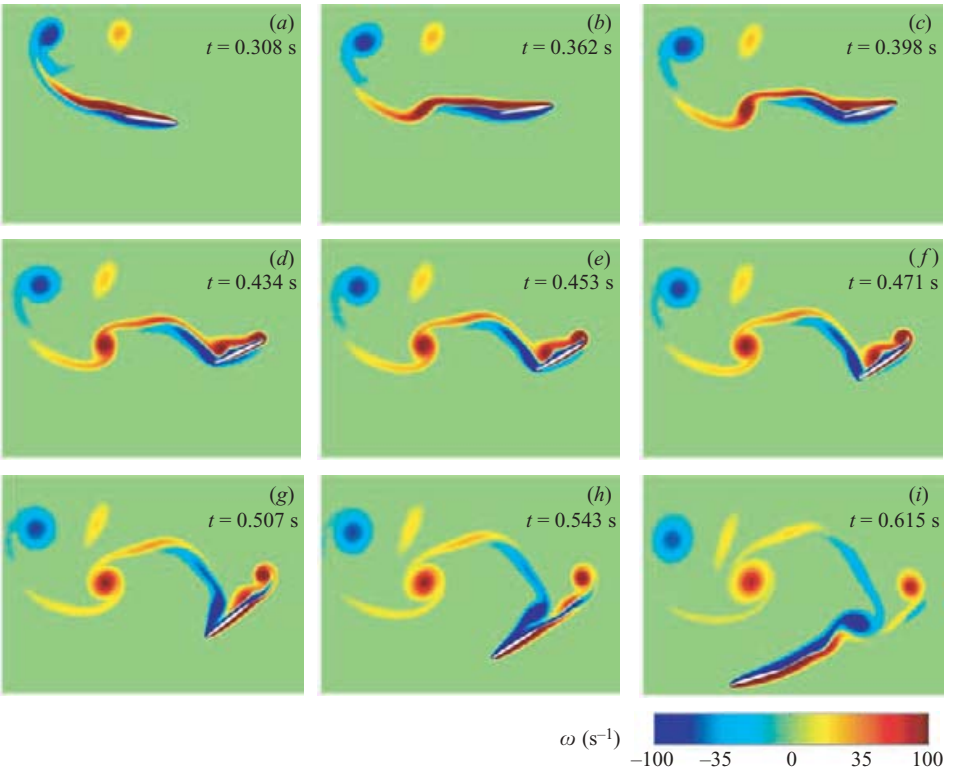

FIGURE 10. The vorticity around the fluttering plate with $\beta = 1/18$, $I^* = 0.057$, and $Re = 412$. The grid resolution was 512×1024. Positive vorticity in red and negative vorticity in blue: (*a*) the plate glides at small angle of attack; (*b*) the plate pitches up and its centre of mass elevates; (*c*) the plate slows down; (*d–f*) the plate turns and starts to shed its old leading edge vortex (red); (*g*, *h*) the old trailing edge vortex (blue) is shed; (*i*) the plate resumes gliding.

unstable, and its centre of mass elevates. The old leading- and trailing-edge vortices are shed as the plate resumes gliding.

6. Fluid forces: measurements and quasi-steady model

6.1. *Experiment and direct numerical simulations*

We extract the fluid force, $\boldsymbol{F}$, and the fluid torque, τ, per unit length on the plate directly from the measured accelerations, i.e. $F_x = m\,\dot{v}_x$, $F_y = m\dot{v}_y + m'\,g$, and $\tau = I\ddot{\theta}$, where $m = \rho_s hl$, $m' = (\rho_s - \rho_f)hl$, and $I = \rho_s hl(l^2 + h^2)/12$. Figure 11 shows F_x, F_y, and τ as functions of the angle θ. The period of oscillation of the plate with elliptical cross-section is shorter than the period of oscillation of the rectangular plate, and for comparison we show the force components and the torque as functions of θ and not as functions of time directly. The measured and the computed forces have qualitatively similar angular dependence and the peak values are comparable. The buoyancy-corrected gravity is $(\rho_s - \rho_f)lhg = 88\,\mathrm{g\,s^{-2}}$ for the rectangular plate and $\pi(\rho_s - \rho_f)lhg/4 = 69\,\mathrm{g\,s^{-2}}$ for the plate with elliptical cross-section. The measured torque is approximately twice as large as the computed torque, but we note that the moment of inertia of the rectangular plate is also approximately twice as large as the moment of inertia of the plate with elliptical cross-section. The computed and the

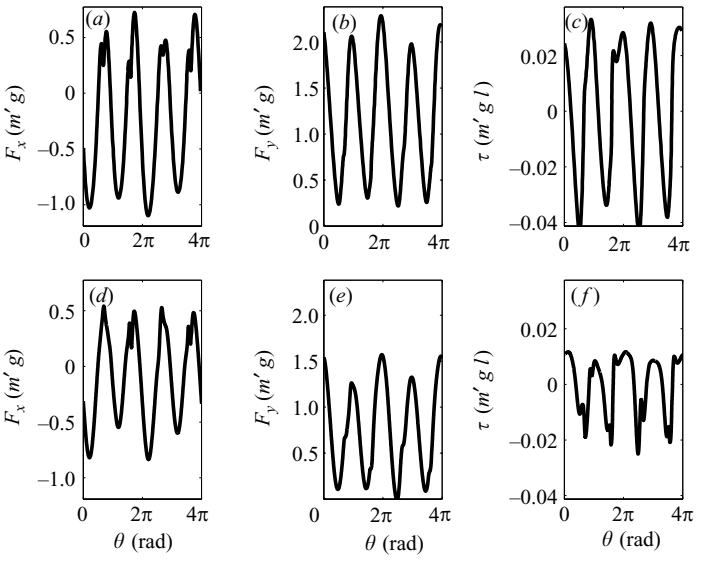

FIGURE 11. The fluid force components and the fluid torque as functions of the angle θ for the tumbling plates with $\beta = 1/8$. (a–c) experiment and (d–f) direct numerical simulation with initial condition I. In both cases we use units where $m' = (\rho_s - \rho_f)hl$. The measured and the computed force and torque are qualitatively similar and we ascribe the quantitative differences between measurements and computations to the differences in geometry.

measured torque normalized by the moment of inertia are therefore comparable. The net fluid force acts close to the centre and the arm of the fluid force is only about 1/100 of the width of the plate. The fluid torque is very small in comparison with the fluid torque on a glider with fixed angle of attack as shown in figure 12 for both small and large angle of attack.

6.2. *Quasi-steady force model*

To quantify the main contributions to the fluid forces we consider a phenomenological model based on ordinary differential equations that without viscous effects reduce to Kirchhoff's equations for a solid body in an inviscid and irrotational flow (Lamb 1945). We write the equations in the coordinate system co-rotating with the plate, and we define $v_{x'}$, $v_{y'}$, and θ as shown in figure 13. The velocity components $v_{x'}$ and $v_{y'}$ are related to the horizontal velocity component, v_x, and the vertical velocity component, v_y, by the transformation: $v_x = v_{x'}\cos\theta - v_{y'}\sin\theta$ and $v_y = v_{x'}\sin\theta + v_{y'}\cos\theta$.

Our model consists of the following set of coupled ordinary differential equations:

$$(m + m_{11})\dot{v}_{x'} = (m + m_{22})\dot{\theta}v_{y'} - \rho_f \Gamma v_{y'} - m'g\sin\theta - F^v_{x'}, \tag{6.1}$$

$$(m + m_{22})\dot{v}_{y'} = -(m + m_{11})\dot{\theta}v_{x'} + \rho_f \Gamma v_{x'} - m'g\cos\theta - F^v_{y'}, \tag{6.2}$$

$$(I + I_a)\ddot{\theta} = (m_{11} - m_{22})v_{x'}v_{y'} + l_\tau \rho_f \Gamma \sqrt{v_{x'}^2 + v_{y'}^2} - \tau^v. \tag{6.3}$$

The terms $m\dot{\theta}v_{y'}$ and $-m\dot{\theta}v_{x'}$ arise due to the co-rotating coordinate system, and the terms involving m_{11}, m_{22}, and I_a are due to added mass effects. The added mass coefficients m_{11} and m_{22}, and the added moment of inertia, I_a, are given by inviscid theory (Sedov 1965). We use the coefficients for a plate with elliptical cross-section:

$$m_{11} = \frac{\pi}{4}\rho_f h^2, \quad m_{22} = \frac{\pi}{4}\rho_f l^2, \quad I_a = \frac{\pi}{128}\rho_f (l^2 - h^2)^2. \tag{6.4}$$

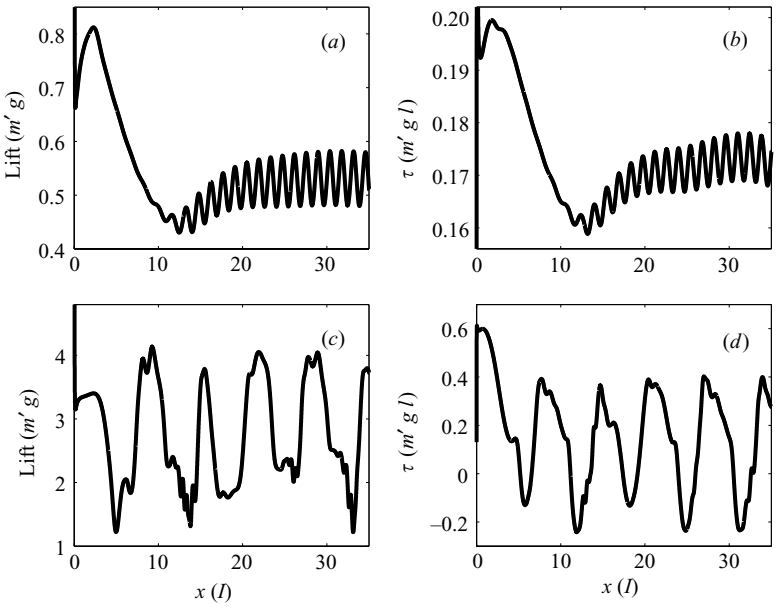

FIGURE 12. The computed lift and fluid torque on steadily translating plates with $\beta = 1/8$ and fixed angle of attack, α, as functions of the distance travelled. The plates were impulsively started and the Reynolds numbers based on the width and the translational speed were 10^3. (a, b) low angle of attack $\alpha = 10^\circ$ and (c, d) high angle of attack $\alpha = 40^\circ$. The torques are one to two orders of magnitude larger than the torques on the freely falling plates in figure 11.

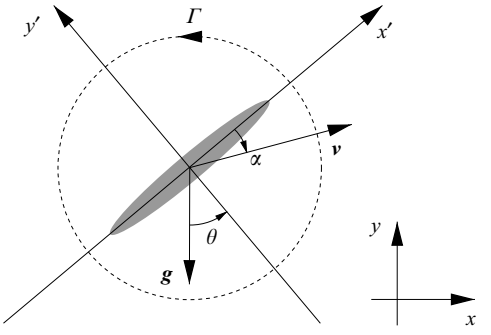

FIGURE 13. The velocity components $v_{x'}$ and $v_{y'}$ in the laboratory reference frame are defined with respect to the coordinate system following the rotation of the body, whereas v_x and v_y are the horizontal and the vertical velocity component in the laboratory reference frame, respectively. The angle of attack, α, satisfies $\alpha \in [-\pi/2, \pi/2]$ and it is negative in the example sketched.

The lift is orthogonal to the direction of motion and proportional to the circulation, $\Gamma = \Gamma(v_{x'}, v_{y'}, \dot{\theta})$, and the drag, $\boldsymbol{F}^v = \boldsymbol{F}^v(v_{x'}, v_{y'}, \dot{\theta})$, and the dissipative fluid torque, $\tau^v = \tau^v(v_{x'}, v_{y'}, \dot{\theta})$, are opposite to the direction of translation and rotation, respectively. In classical aerodynamics for wings with fixed angle of attack the fluid forces are conveniently decomposed into lift and drag. The situation is more complicated in fluttering and tumbling, since the centre-of-mass velocity can point in any direction and almost vanishes at the turning points, where the angle of attack is large and the magnitudes of lift and drag are comparable. However, it is nevertheless convenient to use lift and drag terms to model the fluid forces in a quasi-steady model.

The fluid circulation around the plate is not specified in Kirchhoff's equations and it must be modelled to complete equations (6.1)–(6.3). The plate dynamics is characterized by two velocity scales, i.e. the translational velocity and the rotational velocity of the plate, and we assume that the circulation depends on both velocities. We follow Pesavento & Wang (2004) and write the circulation as the sum of a term proportional to the translational speed and a term proportional to the angular velocity of the plate

$$\Gamma = -\tfrac{1}{2}C_T l\sqrt{v_{x'}^2 + v_{y'}^2}\sin 2\alpha + \tfrac{1}{2}C_R l^2\dot{\theta}, \tag{6.5}$$

where α is the angle of attack defined in figure 13, and C_T and C_R are non-dimensional constants. By definition we have $\alpha \in [-\pi/2, \pi/2]$ and the sign convention described in the caption of figure 13. In terms of $v_{x'}$, $v_{y'}$, and $\dot{\theta}$ we write the circulation as follows:

$$\Gamma = -C_T l\frac{v_{x'}v_{y'}}{\sqrt{v_{x'}^2 + v_{y'}^2}} + \frac{1}{2}C_R l^2\dot{\theta}. \tag{6.6}$$

At low angles of attack the translational lift term reduces to the classical Kutta–Joukowski lift for a translating wing with constant angle of attack, and at high angles of attack it takes stall into account (Wang, Birch & Dickinson 2004). The rotational lift term has the same form as the lift on a pitching plate at zero angle of attack for which $C_R = \pi$ as calculated by Munk (1925). In the quasi-steady model we assume that the functional form is valid in general, but we determine C_R by fitting the measured lift.

The present model of the circulation is different from previous models. Mahadevan (1996) assumed a constant circulation, and Tanabe & Kaneko (1994) and Belmonte *et al.* (1998) assumed that $\Gamma = -\pi l(v_{x'}^2 + v_{y'}^2)^{1/2}\sin\alpha$, i.e. the classical Kutta–Joukowski model. We show in the following that neither of the previous lift models can account for the measured lift, and that the rotational lift dominates in tumbling.

The term $l_\tau \rho_f \Gamma(v_{x'}^2 + v_{y'}^2)^{1/2}$ describes the torque due to the translational and rotational lift. For a plate with elliptical cross-section in an ideal fluid with constant circulation we have $l_\tau = 0$, and for a translating wing at low angle of attack satisfying the Kutta condition we have $l_\tau = l/4$. In § 6.4 we compare the contributions to the fluid torque with the measured torque and discuss the value of l_τ further.

We describe the drag using a standard model, which is valid for a translating wing with constant angle of attack at intermediate Reynolds number (Wang *et al.* 2004). The drag model is quadratic in the translational velocity and it has the following dependence on the angle of attack:

$$\boldsymbol{F}^v = \tfrac{1}{2}\rho_f l[C_D(0)\cos^2\alpha + C_D(\pi/2)\sin^2\alpha]\sqrt{v_{x'}^2 + v_{y'}^2}(v_{x'}, v_{y'}), \tag{6.7}$$

where $C_D(0)$ and $C_D(\pi/2)$ are the drag coefficients at $\alpha = 0$ and $\alpha = \pi/2$, respectively. The model of the pressure contribution to the drag can be motivated theoretically by assuming that the local drag on the plate is proportional to the square of the local velocity component normal to the plate

$$\mathrm{d}\boldsymbol{F}^v = \tfrac{1}{2}\rho_f C_D(\pi/2)|v_n|v_n(-\sin\theta, \cos\theta)\,\mathrm{d}r, \tag{6.8}$$

where we write the drag components in the laboratory coordinate system and define v_n as the local velocity component normal to the face of plate, i.e. $v_n = v_{y'} + r\dot{\theta}$. We use $-l/2 \leqslant r \leqslant l/2$ to denote the position of a plate segment relative to the centre. In the absence of rotation we obtain the term used in equation (6.7) to model the

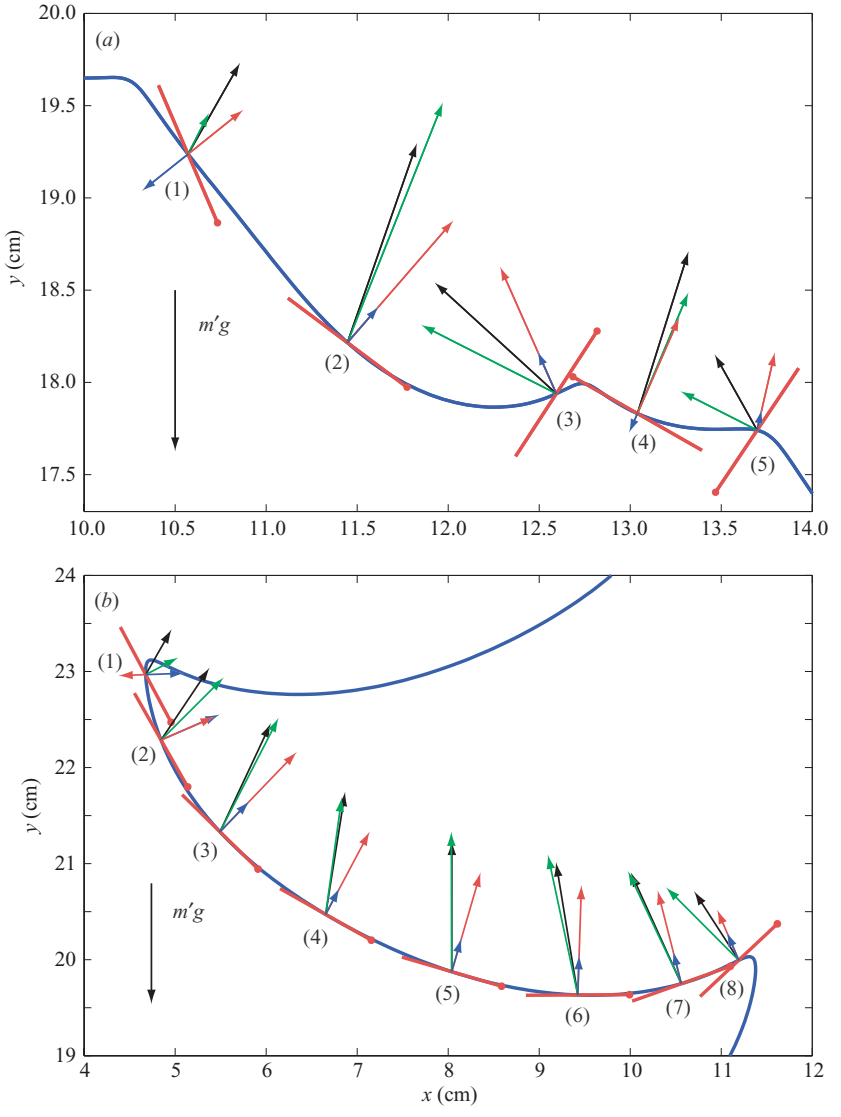

FIGURE 14. Measured fluid force (black), total quasi-steady force (green), translational lift (blue), and rotational lift (red): (*a*) tumbling plate with $\beta = 1/5$ and (*b*) fluttering plate with $\beta = 1/14$. In (*a*) the translational lift points down at (1) and (4) and up at (2), (3), and (5), and the quasi-steady model underestimates the fluid forces at (1) after the short gliding segments.

pressure contribution to the drag

$$\boldsymbol{F}^{v} = \tfrac{1}{2}\rho_f C_D(\pi/2) l \sin^2\alpha \sqrt{v_{x'}^2 + v_{y'}^2}(v_{x'}, v_{y'}). \tag{6.9}$$

In the following we apply the local drag term (6.8) to describe the dissipative fluid torque

$$\mathrm{d}\tau^{v} = \tfrac{1}{2}\rho_f C_D(\pi/2)|v_n|v_n r\,\mathrm{d}r, \tag{6.10}$$

and by integration we obtain the dissipative torque model

$$\tau^{v} = \tfrac{1}{2}\rho_f C_D(\pi/2)\int_{-l/2}^{l/2} |v_n|v_n r\,\mathrm{d}r. \tag{6.11}$$

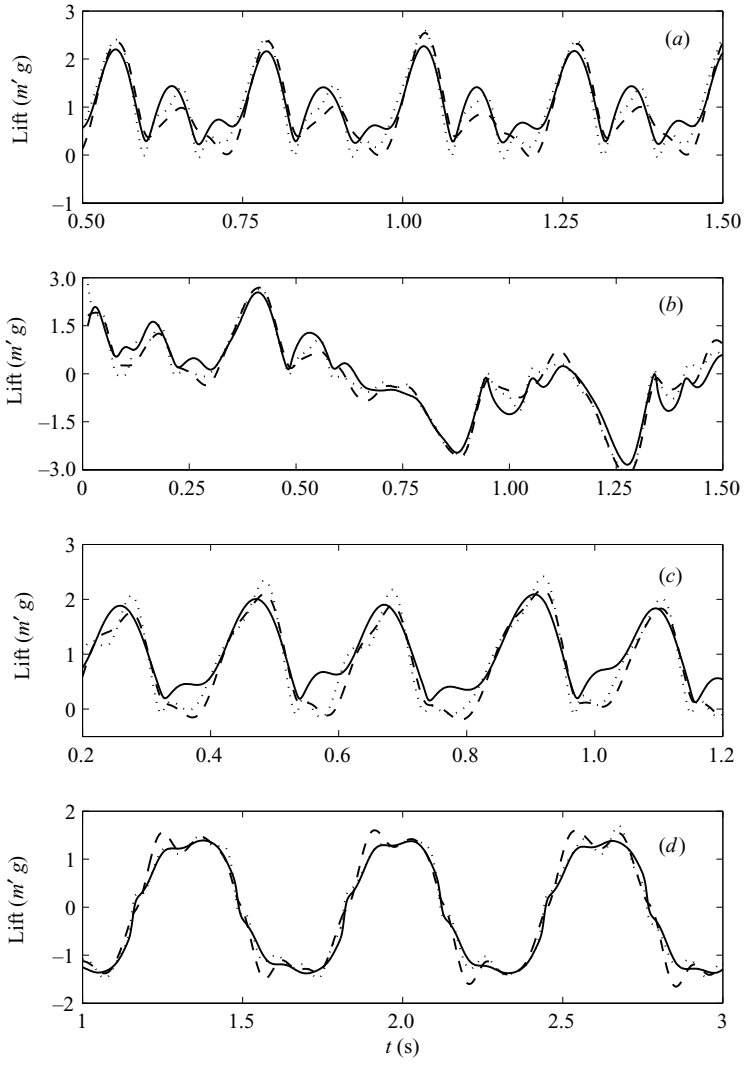

FIGURE 15. Measured lift (solid line), total quasi-steady lift (dotted line), and quasi-steady lift without added mass (dashed line): (*a*) tumbling with $\beta = 1/5$, (*b*) apparently chaotic motion with $\beta = 1/6$, (*c*) tumbling with $\beta = 1/8$, and (*d*) fluttering with $\beta = 1/14$. Added mass effects give negligible contributions to the lift. In (*d*) the sign of the lift defined in equation (6.12) depends on whether the plate moves left or right during the fluttering motion.

β	C_T	C_R	$C_D(0)$	$C_D(\pi/2)$
1/5	1.0	1.4	0.28	2.0
1/6	1.0	1.2	0.15	2.0
1/8	1.0	1.0	0.13	2.0
1/14	1.0	1.1	0.08	2.0

TABLE 4. Lift and drag coefficients in the quasi-steady model.

The torque term vanishes for a purely translating plate, and in the absence of translation we can directly perform the integral: $\tau^{\nu} = (1/64)\rho_f C_D(\pi/2) l^4 |\dot{\theta}|\dot{\theta}$. In § 6.4 we compare this dissipative torque with the fluid torque inferred from experiment.

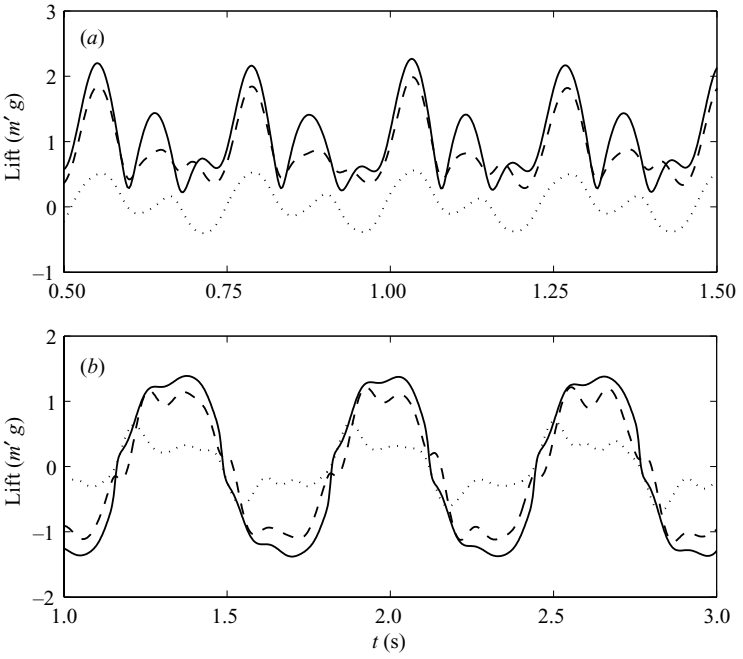

FIGURE 16. Measured (solid line), translational (dotted line), and rotational lift (dashed line): (*a*) tumbling with $\beta = 1/5$ and (*b*) fluttering with $\beta = 1/14$. In (*a*) the average value of the translational lift is small and its functional form is markedly different from the measured lift, whereas the rotational lift captures the main features of the measurements. In (*b*) both translational and rotational lift have significant contributions and the functional forms are similar.

There are two main types of effects which are not accounted for in the quasi-steady approximation, i.e. unsteady corrections to specific force terms and effects due to the interaction of the plate with existing vortex structures. The first type of effects include development of lift during acceleration from rest (Wagner 1925; Pullin & Wang 2004) and unsteady forces due to vortex shedding when a plate is translating at high angle of attack as shown in figure 12. The second type of effects can be significant when the quasi-steady approximation is applied to problems like hovering flapping flight in which a wing is oscillated back and forth and moves into its own wake (Dickinson, Lehmann & Sane 1999). However, a freely falling plate does not interact with its own wake during gliding and such effects are of little significance except at the turning points.

6.3. *Measured and quasi-steady fluid forces*

Figure 14 shows the measured and the quasi-steady force vectors at different instances during tumbling and fluttering. The quasi-steady model describes the measured fluid forces well during most parts of the trajectories, but underestimates the fluid forces immediately after the 180° rotations following the short gliding segments at position (1) in figure 14(*a*). This is to be expected since the plate velocities are small and the wake effects are strong (see figure 9(*h*) for illustration of the wake structure).

Figures 15 and 17 show the measured and the quasi-steady lift and drag as functions of time. We decompose the buoyancy-corrected fluid force, $\boldsymbol{F}$, into lift and drag, $\boldsymbol{F} = \boldsymbol{L} + \boldsymbol{D}$, where we define the lift, $\boldsymbol{L}$, the drag, $\boldsymbol{D}$, and their magnitudes L and D

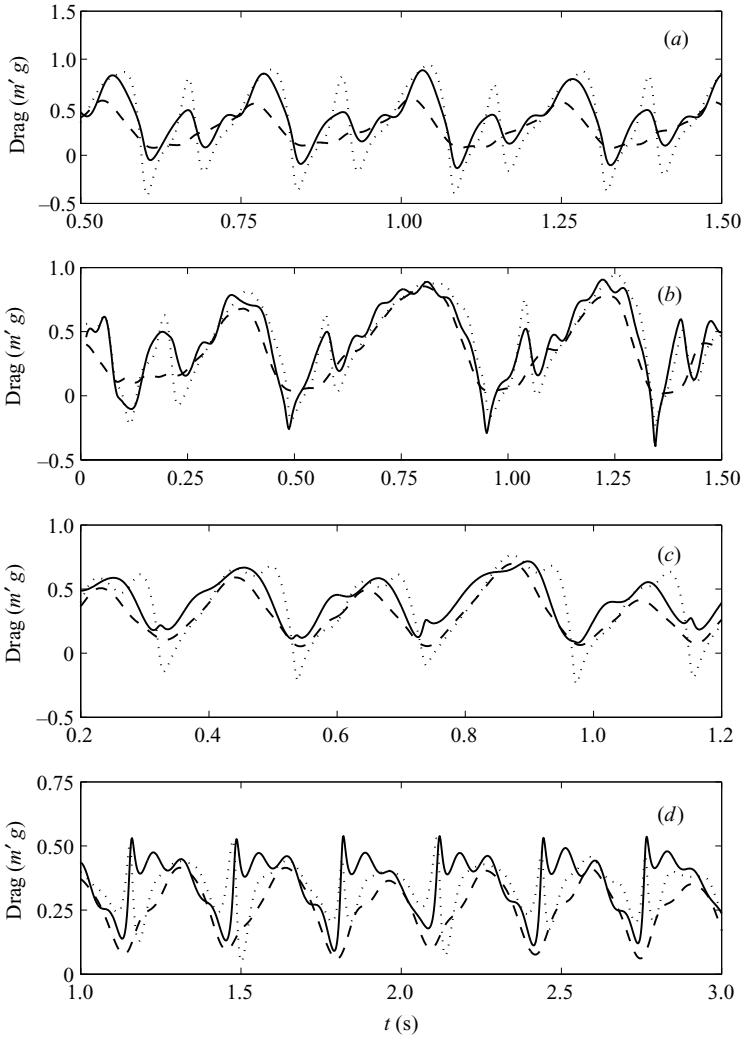

FIGURE 17. Measured drag (solid line), total quasi-steady drag (dotted line), and quasi-steady drag without added mass (dashed line): (*a*) tumbling with $\beta = 1/5$, (*b*) apparently chaotic motion with $\beta = 1/6$, (*c*) tumbling with $\beta = 1/8$, and (*d*) fluttering with $\beta = 1/14$. The relative contributions of added mass effects to the drag are significant, but the resulting thrust peaks (negative drag) are not always observed experimentally as for tumbling in (*c*).

as follows:

$$\boldsymbol{L} = (\boldsymbol{e}_v \times \boldsymbol{F}) \times \boldsymbol{e}_v = L\boldsymbol{e}_z \times \boldsymbol{e}_v, \qquad \boldsymbol{D} = (\boldsymbol{F} \cdot \boldsymbol{e}_v)\, \boldsymbol{e}_v = -D\, \boldsymbol{e}_v. \tag{6.12}$$

We let $\boldsymbol{e}_v$ denote a unit vector in the direction of the centre-of-mass velocity and $\boldsymbol{e}_z$ a unit vector in the z-direction orthogonal to the plane of motion. Positive and negative values of D correspond to drag and thrust, respectively.

The quasi-steady model includes four lift terms, i.e. translational and rotational lift as shown in equation (6.6) with coefficients C_T and C_R, respectively, and translational and rotational added mass terms. We use $C_T = 1.0$ in all four experimental cases and fit the measured lift to obtain the value of C_R. The procedure gives the lift coefficients summarized in table 4, and the quasi-steady lift plotted together with

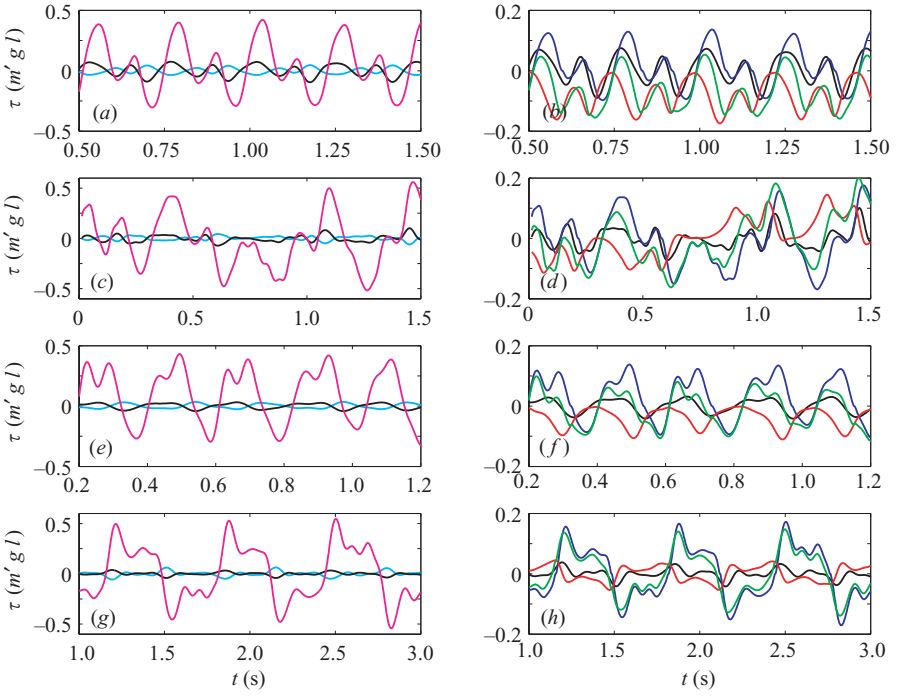

FIGURE 18. Measured torque and quasi-steady torque contributions. Measured torque (black), the term $(m_{11} - m_{22})v_{x'}v_{y'}$ from ideal fluid theory (magenta), the term $-I_a\ddot{\theta}$ related to the added moment of inertia (cyan), the torque from translational lift (blue), the dissipative torque (red), and the sum of the torque from translational lift and dissipative effects (green): (a, b) tumbling with $\beta = 1/5$, (c, d) apparently chaotic motion with $\beta = 1/6$, (e, f) tumbling with $\beta = 1/8$, and (g, h) fluttering with $\beta = 1/14$.

the measured lift in figures 14 and 15. In tumbling the translational lift alternates between pointing up and down with respect to the plate velocity as the plate pitches up at points marked (2), (3), and (5) and down at points marked (1) and (4) as shown in figure 14(a). The average vertical component of the translational lift is thus only 5% of the buoyancy-corrected gravity, and an unrealistically high translational lift coefficient of $C_T = 20$ would be required for the quasi-steady forces to balance the buoyancy-corrected gravity if rotational lift were neglected. In tumbling the quality of the fit of the lift is therefore not very sensitive to the value of C_T, and with values of $C_T = 0.5$ and $C_T = 1.5$ we obtain similar values of C_R as with $C_T = 1.0$. For the fluttering plate shown in figure 14(b) the translational and rotational lift balance 30% and 70% of the buoyancy-corrected gravity, respectively. We note that the lift contribution of added mass is small for both tumbling and fluttering in comparison with the measured lift as shown in figure 15.

The difference between the rotational and the translational lift is further illustrated in figure 16 which shows the translational and the rotational lift contributions together with the measured lift as functions of time. Figure 16(a) shows tumbling with $\beta = 1/5$ for which the functional form of the rotational lift resembles the functional form of the measured lift, whereas the translational lift has a markedly different functional form with approximately zero average. Figure 16(b) shows fluttering with $\beta = 1/14$ for which both the rotational and the translational lift provide important contributions to the total lift and the functional forms are similar.

We model the drag using equation (6.7) with $C_D(\pi/2) = 2.0$ and $C_D(0)$ determined by the best possible fit to the measured drag. We expect that the drag model performs well during gliding at small angle of attack, see figure 14(*b*) positions (3)–(7), whereas we expect that it does not capture the wake-dominated fluid forces at the turning points, see figure 14(*b*) positions (1) and (8). The values of $C_D(0)$ are in the range 0.1–0.3, and the value of $C_D(0)$ decreases with decreasing thickness-to-width ratio as expected. The quasi-steady model predicts added mass effects to overcome viscous drag and result in a net thrust at the turning points for the plates with $\beta = 1/5$, $\beta = 1/6$, and $\beta = 1/8$ as shown in figure 17. A net thrust is also observed experimentally with $\beta = 1/5$ and $\beta = 1/6$, but the magnitude is smaller. An estimate of the added mass coefficients based on the thrust peaks yields coefficients about 50% smaller than the inviscid values.

6.4. *Measured and quasi-steady fluid torque*

Figure 18 shows the measured fluid torque (black) in comparison with the torque term, $(m_{11} - m_{22})v_{x'}v_{y'}$, from ideal fluid theory (magenta), the torque term, $-I_a\ddot{\theta}$, related to the added moment of inertia (cyan), the torque from the translational lift acting halfway between the leading edge and the centre of the plate (blue), the dissipative torque term (red), and the sum of the torque from translational lift and dissipation (green).

The ideal-fluid torque $(m_{11} - m_{22})v_{x'}v_{y'}$ is one to two orders of magnitude larger than the measured fluid torque, and the torque term $-I_a\ddot{\theta}$ is comparable in magnitude to the total measured fluid torque. The forces that produce the $(m_{11} - m_{22})v_{x'}v_{y'}$-term in ideal-fluid theory do not give rise to a net fluid force on the plate, and it is therefore possible for the ideal-fluid torque to be large although the forces due to added mass effects are small. In other words we observe that Kirchhoff's equations in the absence of circulation do not account for the measured lift and overestimate the fluid torque significantly.

The translational and the rotational lift give rise to fluid torque terms, but the values of l_τ are in general different for the two lift terms and theoretical values are only known in special cases, e.g. $l_\tau = 0$ for a plate with elliptical cross-section in an ideal fluid with constant circulation and $l_\tau = l/4$ for a translating wing at low angle of attack satisfying the Kutta condition. Figure 18 shows the torque from the translational lift with the assumption that the force acts halfway between the leading edge and the centre of the plate, i.e. $l_\tau = l/4$ as in the case of a wing translating with constant and low angle of attack. The magnitude of the translational torque term is between two and four times larger than the magnitude of the measured fluid torque in the four experimental cases, and for fluttering the translational torque term clearly overestimates the measured fluid torque. With the assumption that $l_\tau = l/4$ also for the rotational lift we overestimate the measured torque by one to two orders of magnitude. On the other hand the magnitude of the dissipative torque (6.11) with $C_D(\pi/2) = 2.0$ is comparable with the magnitude of the measured fluid torque in the four experimental cases, and the term provides a possible model of the dissipative part of the fluid torque.

7. Conclusion and outlook

We have presented an experimental and numerical study of the unsteady aerodynamics of freely falling plates in a quasi-two-dimensional flow. We have shown that the fluid forces for both fluttering and tumbling plates are markedly different from the fluid forces on a simple gliding airfoil with constant angle of attack. In particular, the lift is dominated by the rotational velocity of the plate, so that a quasi-steady

model with only translational lift is unable to explain the observed plate trajectories. With the exception of the neighbourhoods of the cusp-like turning points, the fluid forces are described well by our revised quasi-steady model and dominated by rotational lift. The rotational lift provides the main mechanism of coupling between plate translation and rotation, and added mass effects predicted by inviscid theory are small in comparison with the translational and the rotational lift terms and play a negligible role in the plate dynamics.

The total fluid force on a freely falling plate acts close to the centre of mass at about 1/100 of the width from the centre and results in a torque which is one to two orders of magnitude smaller than the torque on a plate translating at the same speed. The quasi-steady model correctly predicts the magnitude of the torque in direct numerical simulations of plates translating steadily with constant and low angle of attack, where the pressure force acts approximately halfway between the leading edge and the plate centre. In contrast the fluid torque on a freely falling plate does not build up to a similarly large value, since the plate is free to rotate, and the fluid torque therefore depends sensitively on the precise locations of vortices and low-pressure regions relative to the plate. For these reasons it is more difficult to apply the quasi-steady approximation to model the fluid torque than to model the fluid forces on freely falling plates.

By varying the three non-dimensional parameters, i.e. the thickness-to-width ratio, the dimensionless moment of inertia, and the Reynolds number, we observed periodic fluttering, periodic tumbling, and apparently chaotic motion. Experimentally we found a transition from fluttering to tumbling with increasing thickness-to-width ratio, and we observed apparently chaotic motion and sensitivity to initial conditions in the transition region. In a separate paper we have investigated the transition further using direct numerical simulations and the quasi-steady model (Andersen *et al*. 2005). We refer to this paper for discussion of the aerodynamics in the transition region and analysis of the bifurcation between fluttering and tumbling in the quasi-steady model.

Far from the transition value, the plates flutter or tumble after short transients and display periodic motion with alternating gliding at low angle of attack and fast rotation and centre-of-mass elevation at the turning points. The periodic dynamics observed experimentally was independent of initial conditions. However, with special choices of the non-dimensional parameters we found numerically that the final periodic solution depends on the initial conditions. It will be interesting to study the dependence on initial conditions further and to clarify under what conditions periodic solutions of freely falling plates depend on initial conditions and whether or not chaotic dynamics is possible.

We thank Steve Keast for technical assistance with the construction of the experimental setup and Sheng Xu for many valuable comments and suggestions. This work was supported by NSF, ONR, AFOSR, and the Packard Foundation.

REFERENCES

Andersen, A., Pesavento, U. & Wang, Z. J. 2005 Analysis of transitions between fluttering, tumbling and steady descent of falling cards. *J. Fluid Mech.* **541**, 91–104.

Augspurger, C. K. 1986 Morphology and dispersal potential of wind-dispersed diaspores of neotropical trees. *Am. J. Bot.* **73**, 353–363.

Belmonte, A., Eisenberg, H. & Moses, E. 1998 From flutter to tumble: inertial drag and Froude similarity in falling paper. *Phys. Rev. Lett.* **81**, 345–348.

Dickinson, M. H. 1996 Unsteady mechanisms of force generation in aquatic and aerial locomotion. *Am. Zool.* **36**, 537–554.

Dickinson, M. H., Lehmann, F.-O. & Sane, S. P. 1999 Wing rotation and the aerodynamic basis of insect flight. *Science* **284**, 1954–1960.

Dupleich, P. 1941 Rotation in free fall of rectangular wings of elongated shape. *NACA Tech. Memo.* **1201**, 1–99.

E, W. & Liu, J.-G. 1996 Essentially compact schemes for unsteady viscous incompressible flows. *J. Comput. Phys.* **126**, 122–138.

Ellington, C. P. 1984 The aerodynamics of hovering insect flight. I–VI. *Phil. Trans. R. Soc. Lond.* B **305**, 1–181

Field, S. B., Klaus, M., Moore, M. G. & Nori, F. 1997 Chaotic dynamics of falling disks. *Nature* **388**, 252–254.

Jones, M. A. & Shelley, M. J. 2005 Falling cards. *J. Fluid Mech.* **540**, 393–425.

Lamb, H. 1945 *Hydrodynamics.* Dover.

Lugt, H. J. 1983 Autorotation. *Annu. Rev. Fluid Mech.* **15**, 123–147.

Lugt, H. J. & Haussling, H. J. 1974 Laminar flow past an abruptly accelerated elliptic cylinder at 45° incidence. *J. Fluid Mech.* **65**, 711–734.

Magnaudet, J. & Eames, I. 2000 The motion of high-Reynolds-number bubbles in inhomogeneous flows. *Annu. Rev. Fluid Mech.* **32**, 659–708.

Mahadevan, L. 1996 Tumbling of a falling card. *C. R. Acad. Sci. Paris* **323**, 729–736.

Mahadevan, L., Ryu, W. S. & Samuel, A. D. T. 1999 Tumbling cards. *Phys. Fluids* **11**, 1–3.

Maxwell, J. C. 1854 On a particular case of the descent of a heavy body in a resisting medium. *Camb. Dublin Math. J.* **9**, 145–148.

McCutchen, C. W. 1977 The spinning rotation of ash and tulip tree samaras. *Science* **197**, 691–692.

Munk, M. M. 1925 Note on the air forces on a wing caused by pitching. *NACA Tech. Notes* **217**, 1–6.

Pesavento, U. & Wang, Z. J. 2004 Falling paper: Navier–Stokes solutions, model of fluid forces, and center of mass elevation. *Phys. Rev. Lett.* **93**, 144501.

Pullin, D. I. & Wang, Z. J. 2004 Unsteady forces on an accelerating plate and application to hovering insect flight. *J. Fluid Mech.* **509**, 1–21.

Sane, S. P. 2003 The aerodynamics of insect flight. *J. Expl Biol.* **206**, 4191–4208.

Sedov, L. I. 1965 *Two-Dimensional Problems in Hydrodynamics and Aerodynamics.* Interscience Publishers.

Skews, B. W. 1990 Autorotation of rectangular plates. *J. Fluid Mech.* **217**, 33–40.

Skews, B. W. 1991 Autorotation of many-sided bodies in an airstream. *Nature* **352**, 512–513.

Smith, E. H. 1971 Autorotating wings: an experimental investigation. *J. Fluid Mech.* **50**, 513–534.

Tanabe, Y. & Kaneko, K. 1994 Behavior of a falling paper. *Phys. Rev. Lett.* **73**, 1372–1375.

Wagner, H. 1925 Über die Entstehung des dynamischen Auftriebes von Tragflügeln. *Z. Angew. Math. Mech.* **5**, 17–35.

Wang, Z. J. 2000 Vortex shedding and frequency selection in flapping flight. *J. Fluid Mech.* **410**, 323–341.

Wang, Z. J. 2005 Dissecting insect flight. *Annu. Rev. Fluid Mech.* **37**, 183–210.

Wang, Z. J., Birch, J. M. & Dickinson, M. H. 2004 Unsteady forces and flows in low Reynolds number hovering flight: two-dimensional computations *vs* robotic wing experiments. *J. Expl Biol.* **207**, 449–460.

Weis-Fogh, T. & Jensen, M. 1956 Biology and physics of locust flight I. Basic principles in insect flight. A critical review. *Phil. Trans. R. Soc. Lond.* B **239**, 415–458.

Willmarth, W. W., Hawk, N. E. & Harvey, R. L. 1964 Steady and unsteady motions and wakes of freely falling disks. *Phys. Fluids* **7**, 197–208.